

Micro-Precision Interferometer: A method to evaluate disturbance isolation solutions

Renaud Goullioud^a, Allen Bronowicki^b and Gregory W. Neat^a

^aJet Propulsion Laboratory, California Institute of Technology, CA 91009, Pasadena, USA

^bTRW Space & Electronics Group, CA 90278, Redondo Beach, USA

ABSTRACT

This paper describes a benchmark to assess performance of six-axis vibration isolation systems. The targeted application, spaceborne optical interferometers, requires isolation of reaction wheel disturbances in order to stabilize the precision optical elements to the nanometer level. The problem is to isolate spacecraft vibrations from the precision structure which supports the distributed optical instrument. A corollary challenge is to measure the residual motions in a noisy laboratory environment. The unique feature of this procedure is that isolator performance is measured in terms of the stability of the interferometer optical elements.

Central to the procedure is the Micro-Precision Interferometer (MPI) testbed, which is a hardware model of a future spaceborne optical interferometer. The isolation system under evaluation is mounted on the testbed and disturbance transfer functions are then measured from the isolator payload to the optical sensor output that must be stabilized. Off-line, the procedure combines these measured testbed transfer functions with an empirical model of the reaction wheel disturbance, in order to predict isolator performance over the entire range of wheel speeds. As an example of its use, the paper applies the procedure to five different vibration disturbance interface conditions: “no” isolator (hard mounted); passive elastomeric isolator; passive hexapod isolator; active hexapod isolator; and “perfect” isolator (no connection other than acoustic). The paper compares the five disturbance interface conditions in two different optical pathlength measurement configurations: isolator operating alone with an open loop optical pathlength measuring system; and isolator operating in conjunction with an active optical pathlength control system.

Keywords: Interferometry, Micro-Precision Interferometer, Vibration Isolation, Hexapod, Vibration Attenuation

1. INTRODUCTION

1.1. Problem Description

Spaceborne optical interferometers use an array of two or more small telescopes, as opposed to a single large telescope, to collect light from a single target star. The light from these telescopes, or sub-apertures, is combined to create an interference fringe pattern. This pattern is caused by optical path differences when the distances through each arm of the interferometer from the observed star to the beam combiner/detector are equal to within a few wavelengths of light. These path lengths must be stabilized to the 10 nanometer level in astrometric mode for measurement of stellar angles at sub-milli-arc-second accuracy. The optical paths must be stable to the 1 nm level when nulling starlight to allow imaging of faint planets close to the observed star.¹

The Space Interferometer Mission (SIM) is a first-generation spaceborne interferometer concept with astrometric and imaging goals.² Unlike ground-based interferometers bolted to bedrock,³ instrument optics of SIM are distributed across a 10 m, light-weight flexible structure. The primary mechanical disturbance sources exciting the structure are expected to be the spinning reaction wheels used as actuators for the attitude control system.

Simulation results suggest that in the unattenuated spacecraft environment, the optical path (fringe position) variation is a factor of one hundred above the 10 nm requirement.⁴ This discrepancy inspired the layered vibration attenuation control strategy which involves the blending of vibration isolation, structural quieting, and active optical control. This paper focuses on vibration isolation to assess its contribution to vibration attenuation with and without the active optical control. The isolation system is particularly important in two interferometer operating modes; initial fringe acquisition and observation. During fringe acquisition, the unacquired fringe position must

Other author information: (Send correspondence to Gregory W. Neat)

Gregory W. Neat: E-mail: neat@huey.jpl.nasa.gov

Renaud Goullioud: E-mail: renaud@huey.jpl.nasa.gov

be stable to 80 nm rms. Available vibration attenuation strategies are vibration isolation, structural damping and active optical systems which rely only on internal metrology signals (star light cannot be used to stabilize pathlengths before the star is acquired). During observation, the fringe position must be stable to 10 nm rms for astrometry and 1 nm for nulling. However in this case, the vibration attenuation suite is increased to include optical systems closed on the actual stellar signal. The active optical delay line implements low-to-mid frequency pathlength control which removes the majority of rigid body attitude control and low frequency structural motions.

1.2. Background

Evaluating the vibration attenuation control strategy in a ground test environment implies an additional challenge of accurately representing the on-orbit disturbance conditions while avoiding ground-based noise sources such as acoustics and seismic motions. Reference⁵ presents an example layered vibration attenuation concept evaluated on a 3 m cantilevered truss structure containing a subset of interferometer optical elements and a uni-directional shaker. Though the optical path through the system was stabilized to 5 nm (RMS), this initial system was primarily rejecting the ambient lab disturbance environment in combination with broadband disturbance inputs from the shaker. The layered strategy utilizing vibration isolation and active optical control was subsequently evaluated on the Micro-Precision Interferometer (MPI) testbed.⁶ The improvements in this hardware validation study were: a suspended and dimensionally representative structure; a six-axis disturbance source; the requisite six-axis vibration isolation capability; and a first generation performance evaluation procedure to assess performance in the anticipated on-orbit disturbance environment.

This paper contributes a refined performance evaluation procedure that has enabled the comparison of different vibration isolation and active optics solutions under dynamic conditions and with metrics that are representative of those expected on-orbit for spaceborne interferometers. The original performance evaluation procedure,⁶ utilized a broadband stochastic disturbance model whereas the approach presented in this paper considers the disturbance source deterministic and narrowband in nature.

Traditionally, performance assessment of vibration isolation systems has been done by measuring transmissibility from the “noisy” side (disturbance payload) to the “quiet” (isolated) side on a test bench.⁷ When the base or the payload experience flexibility, this approach becomes complex to interpret. Although that strategy provides a quantitative technique for assessing isolator performance on its own, the mechanical boundary conditions are not representative of the on-orbit boundary conditions and it is difficult to extrapolate from the transmissibility results to actual instrument performance, especially for six axes of disturbance forces and torques.

1.3. Approach

Central to this performance evaluation procedure is the Micro-Precision Interferometer (MPI) testbed.^{8,9} Figure 1 shows a bird’s eye view of the MPI testbed. Located at the Jet Propulsion Laboratory, the testbed contains all the subsystems necessary to assess the effectiveness of the vibration attenuation technologies. These subsystems are: a 7 m x 7 m x 6.5 m softly suspended truss structure with mounting plates for subsystem hardware; a six-axis vibration isolation system which supports a disturbance source which emulates reaction wheel imperfections; a complete Michelson interferometer; internal and external metrology systems; a star simulator that provides stellar input to the interferometer collecting apertures; fast steering mirrors which can keep the starlight beam focused on the detector; and active optical delay lines which compensate for rigid body and flexible motion of the support structure to maintain equal pathlength between the two interferometer arms.

The procedure involves interfacing the isolator under evaluation to the testbed and measuring the requisite disturbance transfer functions in six degrees of freedom. These transfer functions accurately depict (in a linear sense) the effectiveness of the vibration isolation system at achieving nanometer stabilization of the optical elements. Modeled reaction wheel disturbance profiles are then convolved analytically with this family of measurements to predict the on-orbit performance in terms of the desired metric; nanometers of optical path difference (OPD) as a function of wheel speed. Applying different norms to these performance functions, the performance metric is simplified to a single number. Using the procedure, the paper compares five disturbance source interface conditions. These include perfect isolation (no contact), hard mounted (no isolation), a simple passive elastomeric isolator and a novel passive or active hexapod isolator based on a flight proven passive hexapod design.¹⁰ The paper presents each isolator configuration, the procedure to assess isolator performance and the corresponding results from the evaluation procedure for each configuration.

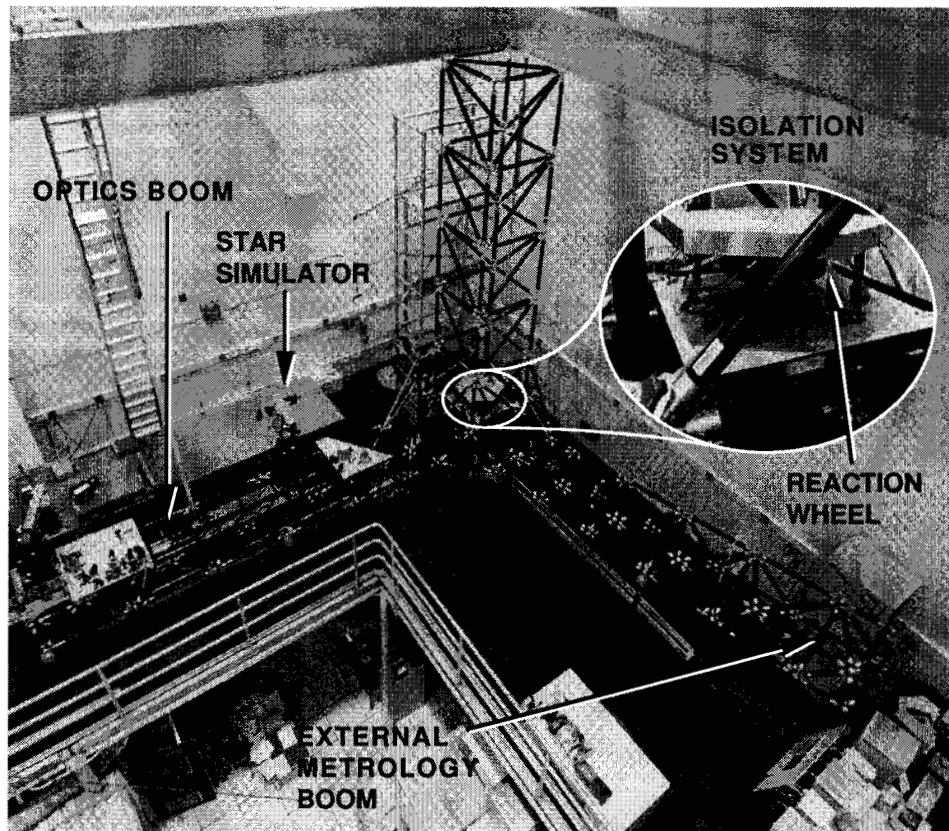


Figure 1. Bird's eye view of the MPI testbed with inset showing a close-up of a six-axis isolation system.

2. ISOLATOR DESCRIPTIONS

This section describes five different impedance configurations between the disturbance source and the structure supporting the interferometer. The connections ranged from no isolation (hard mount), through three kinds of isolation (simple elastomeric isolator, passive and active hexapod), to "perfect" isolation (disturbance suspended from ceiling). In each case, the isolator system under test is located between two plates: the base plate, rigidly mounted to the structure and the payload plate which supports the disturbance source. The payload was constant for each test and weighed 26 kg. The payload consisted of shakers, force sensors and ballast mass in order to approximate the mass and inertia of a single reaction wheel. The location of these two plates is shown in the inset of Figure 1.

2.1. "Perfect" Isolator

Configuration 1 in Figure 2 was used to evaluate the performance of a "perfect" isolator in which there is no mechanical connection to the testbed. In this configuration, a bungee cord suspends the entire disturbance payload from the facility ceiling. Some of the subsequent configurations use the same bungee to minimize the effect of the 1-g gravitational sag on the isolator. The vertical resonant frequency of the suspended assembly was below 1 Hz and the lateral pendulum frequency was approximately 0.3 Hz

This unattached configuration provides a means to quantify the fidelity of the measurement approach. Any signal in the measured transfer function that shows coherence between shaker and OPD indicates the presence of a disturbance path other than through the isolator structure. This path could be through umbilical cables, acoustic transmission of vibrations, or through the structure itself if the shaker payload gravity offload is suspended from the truss rather than the facility ceiling. This configuration was used to identify and eliminate sources of flanking load paths around the isolator. Sound absorbing material was added to the base plate to reduce the acoustic transmission path.

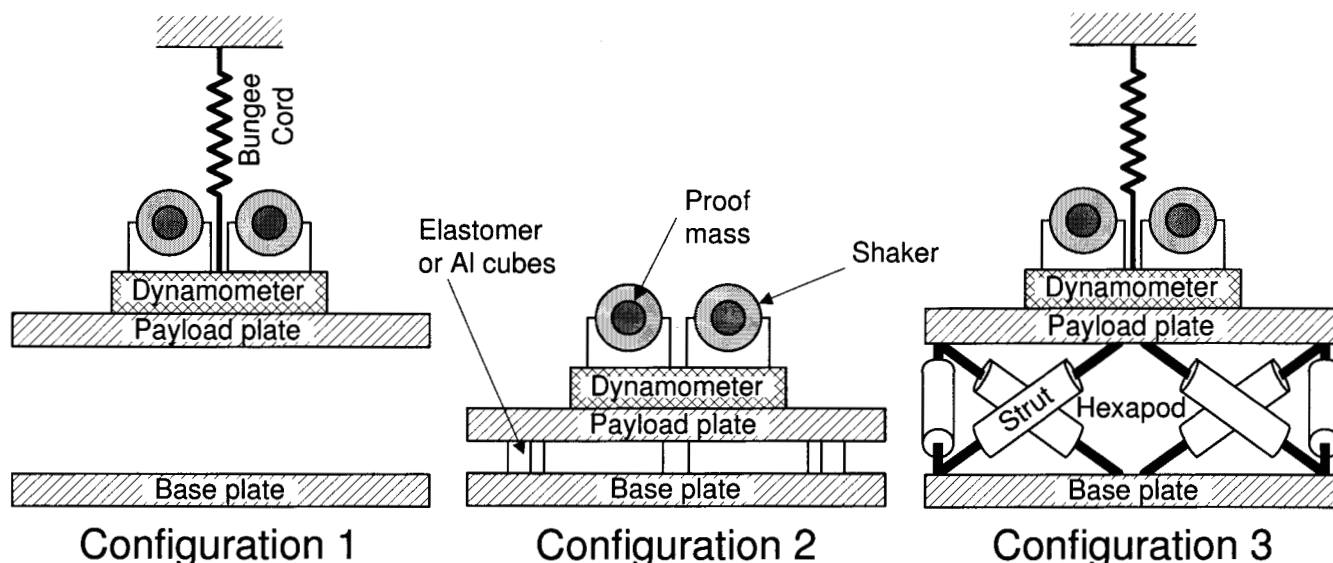


Figure 2. Test configurations used in this study; perfect isolation (configuration 1), hard mount and elastomeric (configuration 2), hexapod active and passive (configuration 3).

Once flanking paths are removed, with the high bandwidth optical system on, the test setup provides a means to quantify the noise floor of the transfer function measurement setup. The lab ambient disturbance environment, the data analyzer and testbed sensors all contribute to the transfer function noise floor. To demonstrate stabilization to the nanometer level requires a system with a noise floor below 1 nm.

2.2. No Isolator (Hard Mounted)

To emulate the hard mounted disturbance configuration, the disturbance payload was bolted to the base plate through three steel cubes (see configuration 2 of Figure 2). The three hard points were situated at the periphery of the payload plate, spaced 120° apart.

In contrast to the “perfect” isolator which provided a lower bound on the transfer function measurement setup, the hard mount configuration provides an upper bound to compare isolation system performance. Correspondingly, these two configurations bound the isolation performance metrics; the perfect isolator providing the lowest and the hard mounted providing the maximum metric values.

2.3. Elastomeric Isolator

The elastomeric isolator also utilizes configuration 2 shown in Figure 2, replacing the steel cubes with three 1 cm cubes made of the vacuum compatible silicone RTV615. Figure 3 shows one of the elastomeric cubes used for the isolator. The cubes were pre-loaded with the 1-g force from the payload plate. They were compressed roughly 30% of their nominal uncompressed length. The passive modes of this configuration are 2 Hz for two lateral sway motions, 4 Hz for torsion, 9 Hz for vertical bounce and 15 Hz for two rocking modes.

This isolator configuration is not a “flight” design at this point. The intention is to use the performance evaluation procedure to compare this prototype isolator concept to the other available isolation schemes. If it demonstrates respectable performance then this concept may advance to a more mature development phase.

2.4. Passive Hexapod Isolator

TRW’s Space & Electronics Group developed a six degree of freedom (DOF) mount capable of passively attenuating vibrations from 10-100 Hz, with at least 10% damping across a broad temperature range. It has very low parasitic stiffness: only 1% of in-line stiffness (loads transmitted through paths that cannot be controlled by sensors and actuators). The system consists of six identical struts arranged in a mutually orthogonal configuration. Each of the isolator struts features a compound main spring to provide axial compliance. A five degrees of freedom fiberglass

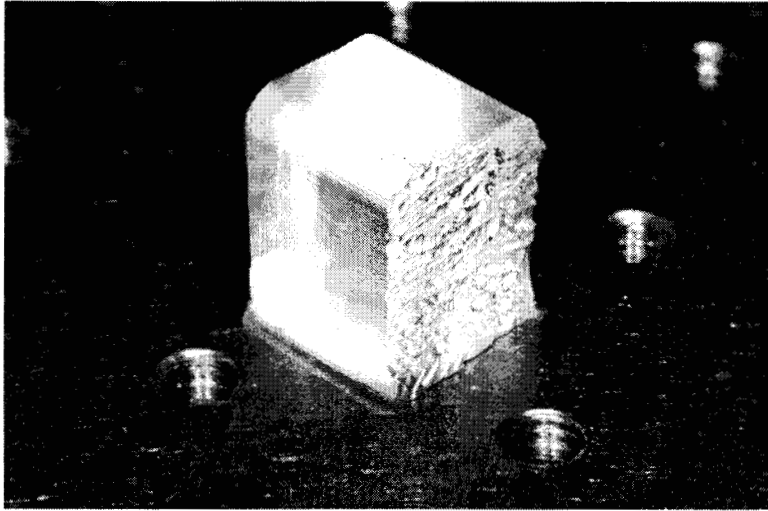


Figure 3. Elastomeric cube Closeup. (table holes are 6 mm in diameter on a 25 mm grid)

rod flexure at the top transmits primarily axial forces. A two degrees of freedom flexure at the bottom, made of a slotted aluminum spring with a pultruded graphite rod bonded on the centerline, is compliant mainly in bending. The flexure arrangement ensures that transmission of torques and side forces is minimal. A closeup view of the active/passive hexapod isolator struts is shown in Figure 4.

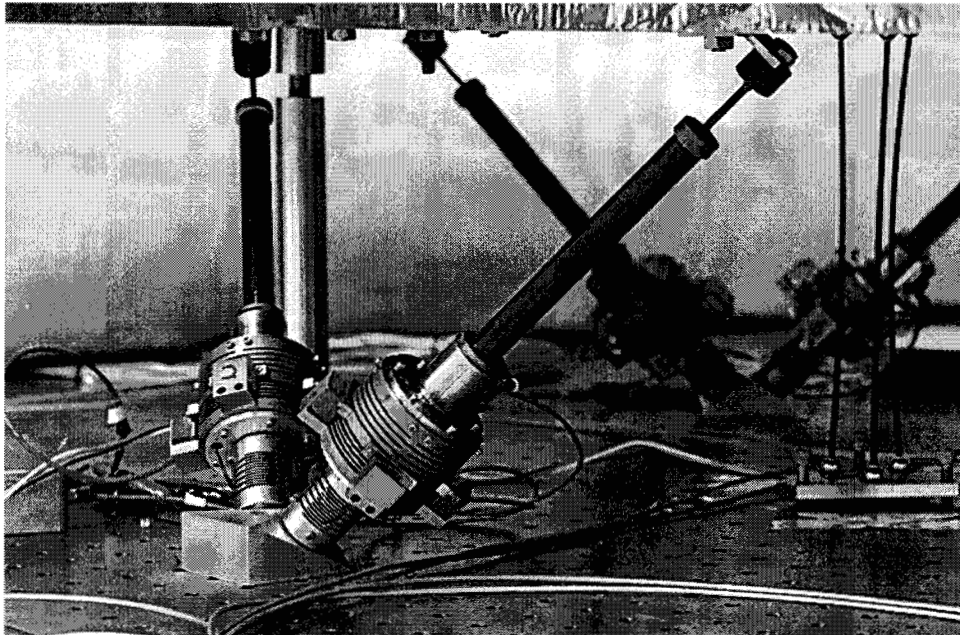


Figure 4. TRW Active/Passive Hexapod Isolator Closeup.

The main spring is a titanium cylinder slotted to produce a series of flexure beams. A set of stiff slots is in series with a softer slotted section. Viscoelastic material (VEM) is situated parallel to the soft slots as shown in Figure 5. Two kinds of VEM, a soft material with a low transition temperature and a harder material with a higher transition temperature, are inserted in series between the blades protruding from the main spring. The blades cause axial deformation in the spring to shear the VEM. The design forces about 40% of the load to go through the VEM at room temperature, the rest through the soft spring section. As temperature drops, the VEMs harden, but the soft VEM still provides damping action, as the proportion of load through the VEM increases. As temperature rises both

VEMs soften, attracting less load, but the loss factor of the stiffer VEM increases. The stiff slotted spring serves to maintain compliance of the isolator at high frequencies, where the VEMs act stiffer. At room temperature, stiffness of the 6 composite springs was measured in the range 103 to 139 pounds/inch, while damping was 19-20%. Damping is predicted to remain above 10% over the range $70^{\circ} \pm 40^{\circ}F$. Stiffness will vary between 250 and 80 pounds/inch at the cold and warm ends, respectively, due to modulus changes in the VEM.

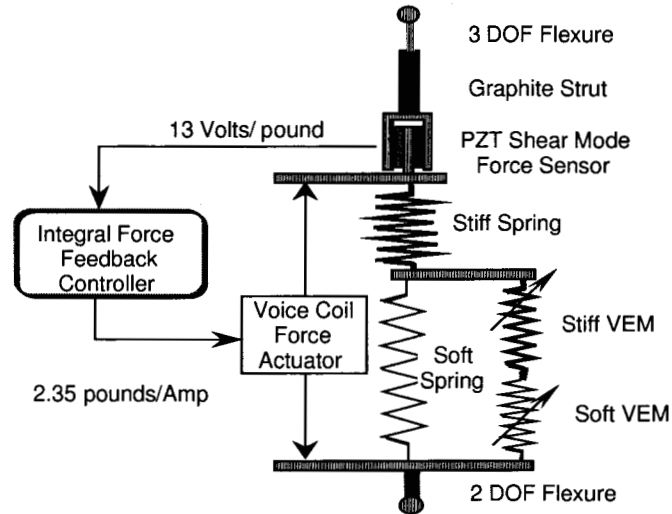


Figure 5. Functional schematic of hexapod isolator strut.

The performance measurement procedure used configuration 3 of Figure 2 to assess the system's passive performance. Note that the configuration utilizes the same off-load bungee used in the "perfect" isolator test. This is necessary since the passive isolator hexapod springs bottom out for a total vertical gravity load around 5 kg. In the space application the gravity effect will not be present. In this configuration, the passive isolation modes of the hexapod are: 4.25 Hz for two lateral sway motions, 9.75 Hz for vertical bounce, 11 Hz for torsion and 15 Hz for the two rocking modes.

2.5. Active Hexapod Isolator

The active hexapod isolator utilized the same hardware described in the passive hexapod isolator, with an additional active feedback loop on each strut. The design thus has a passive backup in case the active isolation fails for some reason. Figure 5 shows the active loop, using a voice coil electromagnetic actuator and a force sensor on each strut for the feedback signal. The voice coils are located inside the titanium springs, acting in parallel with the compound main spring. The actuators deliver 2.35 pounds of force per amp, and are driven by a voltage to current converter. Four Navy Type I PZT shear mode wafers act in parallel as a low-noise sensor measuring force transmitted through the spring. The PZT shear mode is roughly one hundred times less sensitive to pyroelectric effects than the axial or lateral modes, thus mitigating low frequency noise due to thermal transients. A similar approach has been used in piezoelectric accelerometers. Together with a high-gain (100X) charge amplifier, a sensitivity of 13 Volts/pound is achieved. Even in the presence of room acoustics, resolution was measured at 50 micro-pounds.

It was possible to stably implement six single input-single output (SISO) feedback controllers individually on each strut when the payload weight was light enough so that a gravity offload was not needed. It was realized that the offload introduced coupling only in the vertical direction. A decoupling matrix to convert sensed strut forces to global payload x, y, z forces and moments was introduced, so that independent SISO controllers could be implemented in the global space. The simplest means of implementing the decoupling is to use Independent Modal Space Control.¹¹ The IMSC feedback controller was implemented on the Modular Control Patch digital controller.¹² This is a miniaturized control computer measuring 3" by 5", containing analog conversion hardware, digital interface, RAM, ROM and a 32 bit floating point digital signal processor. To simplify testing of the isolation controllers, virtual test points were created, allowing global forces to be measured and also commanded; and allowing individual modal

isolation loops to be broken one at a time. Loop shaping was used to maximize gain around the isolation frequencies, while maintaining stability margins. The active loop augmented the existing passive isolation from 2 to 60 Hz with maximum feedback of 40 dB around 10 Hz.

The performance measurement procedure used configuration 3 of Figure 2 to assess the system's active performance in the same manner as the passive TRW isolator. In this configuration, the active isolation modes of the hexapod are: 2 Hz for two lateral sway motions, 4 Hz for vertical bounce, 6 Hz for torsion and 8 Hz for the two rocking modes.

3. ISOLATOR PERFORMANCE EVALUATION

3.1. Procedure Overview

Isolator performance is evaluated by combining disturbance transfer functions measured on the testbed with an analytical disturbance model. This hybrid experimental/analytical procedure allows one to predict on-orbit performance over an entire range of disturbance conditions in an accurate, efficient manner. One set of transfer function measurements can be convolved analytically with any combination of speeds of the four reaction wheels which would reside on the isolated platform of a real spacecraft.

Measuring performance solely in hardware would require measuring the optical metric while stepping through all combinations of wheel speeds for the four reaction wheel assemblies. The time required to perform those measurements is prohibitive. Torques from spinning actual wheels up and down would require a separate attitude stabilization system be applied to the soft, zero-gravity simulating suspension system. That would likely involve at least one compensating reaction wheel. Perhaps most important, if one used actual reaction wheels, ambient lab disturbances would corrupt the optical sensor data, since the isolated reaction wheel disturbances would be extremely low. Ambient disturbances not traceable to space include low frequency motion of the suspended structure, pseudo-star motion, atmospheric effects on the laser beams, and room acoustics.

Conversely, assessing performance solely in analysis would require an accurate analytical representation (over all frequencies) of the structure, control system sensors and actuators and the disturbance sources. Attaining the necessary model fidelity is a challenge; especially at higher frequencies (100 Hz).¹³ In addition, it is difficult to accurately represent the actuators and sensors, particularly with respect to practical implementation constraints such as noise floors and dynamic ranges.

Figure 6 shows how the task of accurately representing the on-orbit problem has been distributed between the hardware and analysis tools. The four steps which make up this procedure are: (1) the analytical reaction wheel disturbance model, (2) measuring disturbance transfer functions from shakers through isolator to optical sensor, (3) the physical performance prediction algorithm, and (4) the calculation of output optical performance metrics.

3.2. Reaction Wheel Disturbance Model

Based on test data obtained from the Hubble Space Telescope (HST) flight units,⁹ the disturbance forces and torques are modeled as discrete harmonics of the reaction wheel speed, f_{rwa} , with amplitudes proportional to the wheel speed squared:

$$m(t) = \sum_{i=1}^n C_i f_{rwa}^2 \sin(2\pi h_i f_{rwa} t + \phi_i) \quad (1)$$

where $m(t)$ is the disturbance torque or force, C_i is an amplitude coefficient, h_i is the harmonic number, and ϕ_i is a random phase (uniform over $[0, 2\pi]$) used to account for phase uncertainty. According to this model, h_i and C_i uniquely determine the amplitude and frequency of each harmonic component for a given wheel speed.

The disturbances modeled are: one axial force along the wheel spin axis, two radial forces normal to the spin axis, and two radial torques causing wheel wobble. Wheel mass imbalances, commonly known as static imbalance, produce the two radial forces in the fundamental harmonic of wheel speed, which thus have known 90° phase with respect to each other. Wheel product of inertia imbalances, known as dynamic imbalance, produce the two radial torques, also with 90° phase to each other. The remaining disturbances are attributed to bearing imperfections. Disturbance torque about the axis of rotation (torque ripple and motor cogging) was found to be insignificant. Figure 7 shows C_i plotted versus h_i for each of the disturbances.

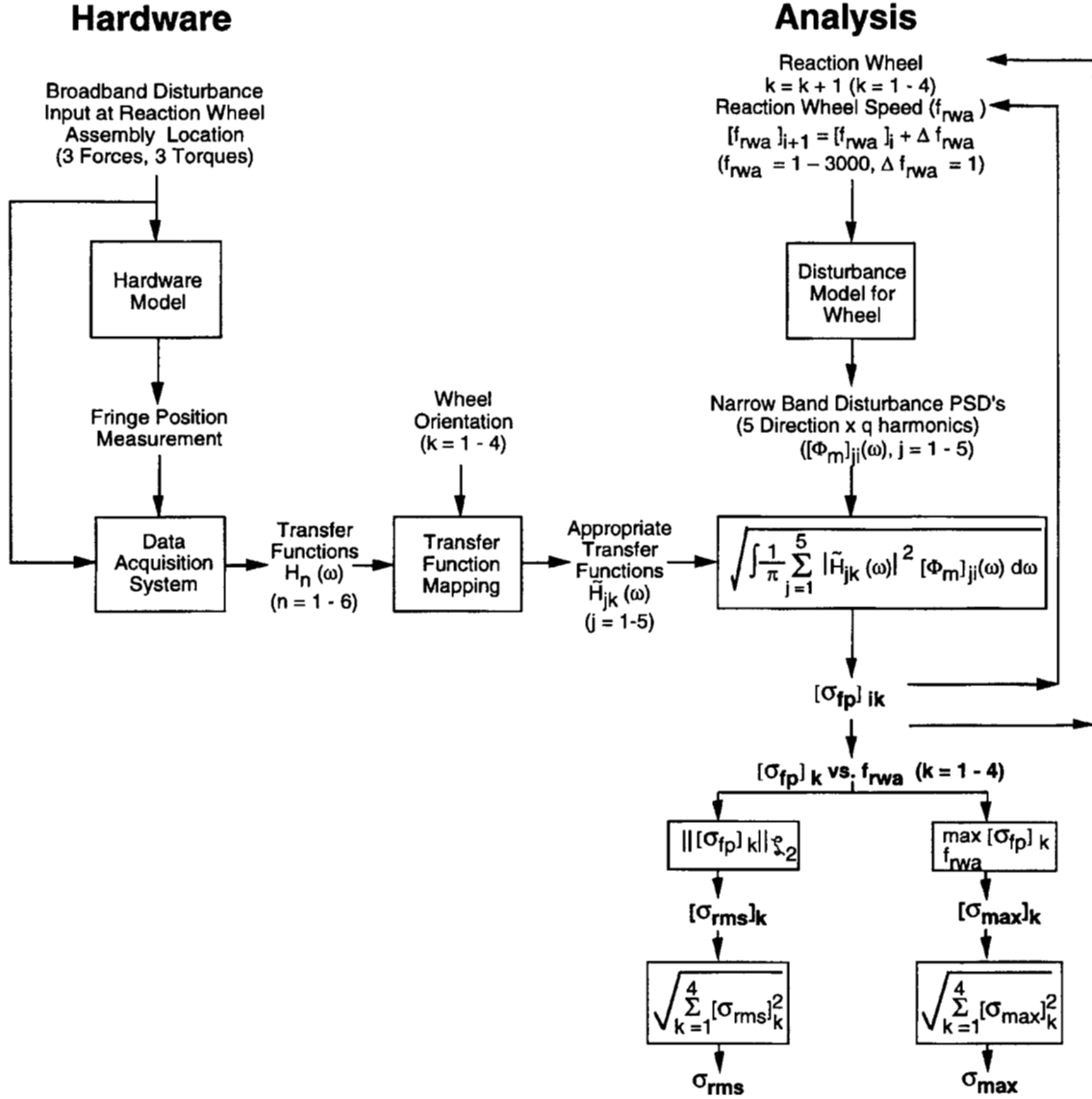


Figure 6. Isolator performance evaluation procedure.

The procedure requires reaction wheel disturbance power spectral densities as input to the measured transfer functions. Given that the reaction wheel disturbances are sinusoidal wheel harmonics (Eq. 1), and assuming that the random phases (ϕ_i) are independent, identically-distributed,¹⁴ the power spectral densities consist of Dirac delta functions¹⁵ at the harmonic frequencies:

$$\Phi_m(\omega) = \sum_{i=1}^n \frac{\pi C_i^2 f_{rwa}^4}{4} [\delta(\omega - 2\pi h_i f_{rwa}) + \delta(\omega + 2\pi h_i f_{rwa})] \quad (2)$$

where $\Phi_m(\omega)$ is the power spectral density of $m(t)$, and $\delta(t)$ is the Dirac delta function.

3.3. Disturbance Transfer Functions

The experimental part of the procedure consists of measuring disturbance transfer functions. These measurements characterize (in a linear sense) how forces and torques applied at a specific location affect the optical output of the instrument. Figure 8 (left side) shows a cartoon of this disturbance propagation path. A known force or

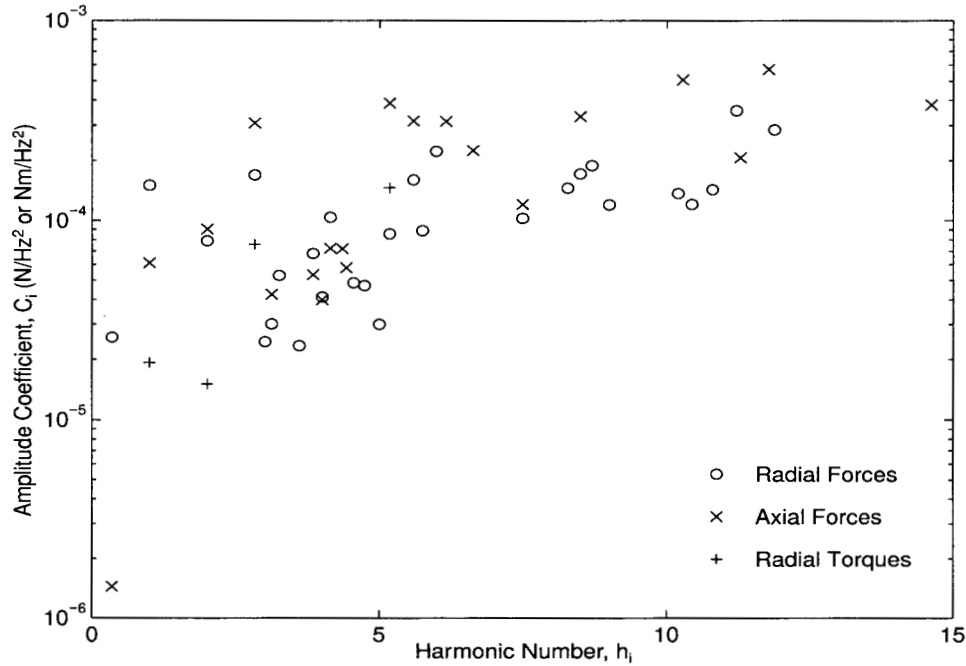


Figure 7. Plot of C_i versus h_i for each reaction wheel disturbance direction (see Eq. 1 for definitions). In general, h_i are not integers.

torque is applied at the reaction wheel mounting location. This disturbance is attenuated by the isolator under evaluation, propagates through the structure and finally rattles the optical elements. The right side of Figure 8 shows a block diagram of the disturbance propagation path along with the external HP data analyzer used to measure the disturbance transfer functions. The following sections discuss how each of the individual elements in Figure 8 contribute to making the transfer function measurement.

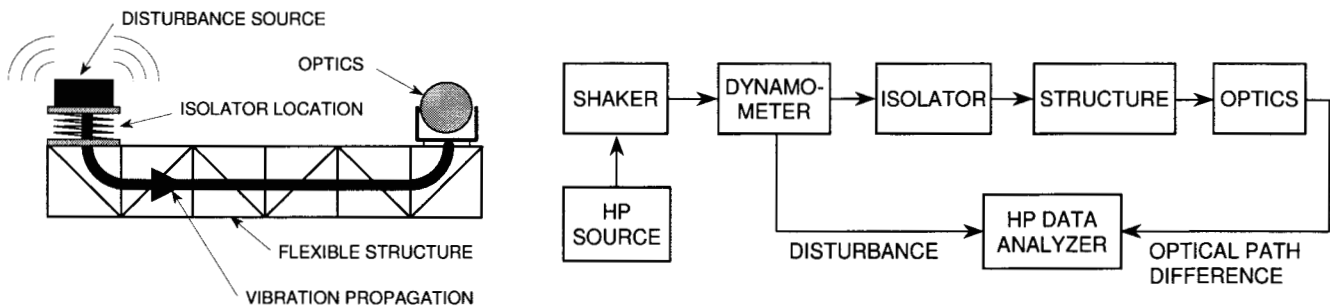


Figure 8. Disturbance vibration propagation associated with the transfer function measurement approach.

3.3.1. Disturbance Payload

The disturbance source consists of a pair of shakers mounted to a custom six-axis force measuring device (dynamometer). Figure 9 shows the dynamometer with the two shakers. The mass of the payload plate, dynamometer, shakers and proof masses together is 26 kg. Forces are produced by driving the shakers in phase, and moments by driving them anti-phase. The shakers are manually re-oriented to measure the six different transfer functions.

The dynamometer is a six degrees of freedom disturbance sensor. The outputs are three forces (X, Y and Z) and

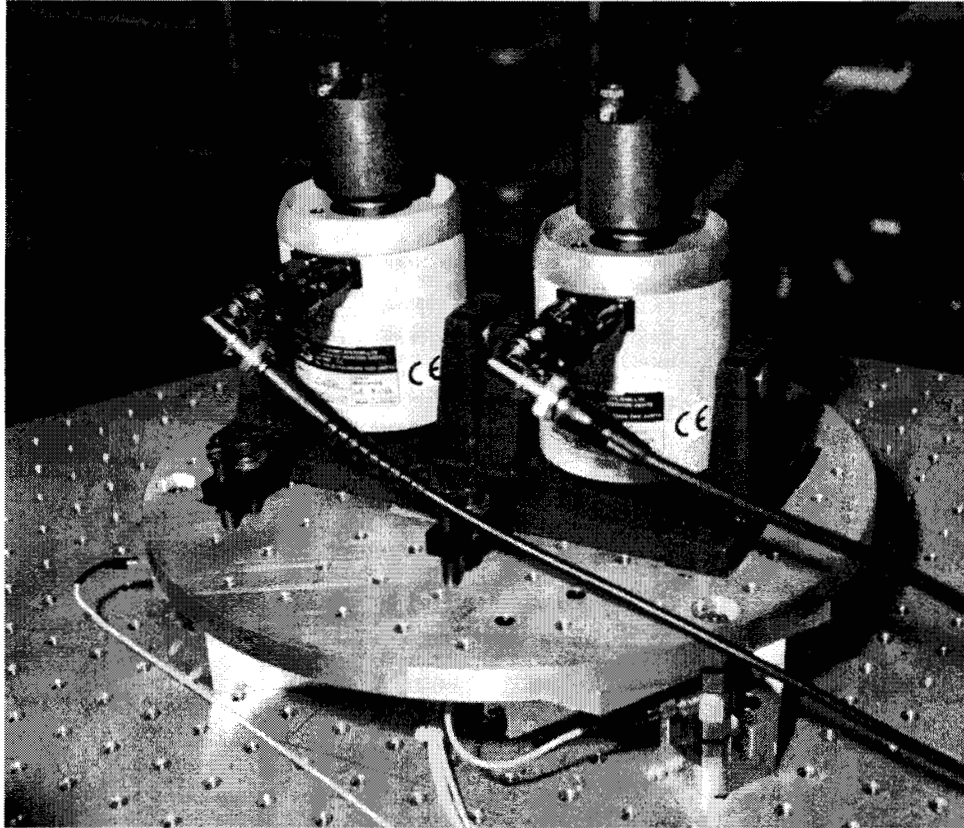


Figure 9. Dynamometer with two linear shakers on the top plate producing a Z force.
A load-cell between two flexures can be seen on the lower right of the picture.

three torques (about X, Y and Z). The mechanical parts consist of the base plate, 6 load cells, 12 flexures and the top plate. The top plate is mounted to the base of the dynamometer only through the six load cells, three in the vertical direction and three in the horizontal one. The load cells are arranged in a triangular configuration. Two flexures are mounted on each side of the load cell to reduce the coupling between load cells. These flexures have to be soft enough to reduce the coupling but stiff enough so that the dynamometer modes are located above the frequency range of interest (750 Hz). Signal conditioning consists of the load cell signal amplifiers and an analog transformation matrix board. This board produces six global outputs (X, Y, Z forces and X, Y, Z torques).

An HP signal analyzer is used to measure disturbance transfer functions. The HP unit generates a broadband drive signal. This signal is sent to the two shakers through two power voltage amplifiers. To generate torques, polarity is inverted to one of the shakers. The bandwidth is divided into 3 ranges (2 - 14.5 Hz, 10 - 110 Hz and 100 - 900 Hz) with driving voltage increasing with the frequency to account partially for isolator attenuation, maintaining signal to noise ratio. The dynamometer signal conditioner produces a voltage proportional to the disturbance. This voltage is sent to the HP analyzer as the input for the transfer function.

3.3.2. Structure

The isolator interface to the structure is a 1 meter square honeycomb plate with aluminum face sheets (see background in Figure 9). This plate is rigidly mounted to the 6m x 6.5m x 5m flexible structure. The truss structure is composed of drawn thin walled 6061-T6 aluminum tubes. The joint design consists of an aluminum node ball interconnecting two or more struts with "b-nut" interface hardware which facilitates simple installation and a mechanism to preload the joints. Six independent kinematically mounted interface plates are distributed across the structure to enable the mounting of the interferometer optical elements. Further details on the structure design and assembly procedures are given in reference.¹⁶ The entire structure is suspended from the ceiling with a CSA passive/active pneumatic/electromagnetic suspension system. The rigid body suspension modes are all below 1 Hz and the first flexible mode of the structure is just below 5 Hz.

The strategy for attacking the vibration attenuation problem was to initially build a lightly damped, linear structure and determine the residual optical error after applying vibration isolation and active optical control. If the requirements were met, active (or passive) structural control might be included in order to increase performance margins. If the requirements were not met, structural control would be added to the vibration attenuation strategy in order to meet requirements. Active optical control was selected initially over structural control since the instrument must have this capability anyway to reject low frequency attitude control and thermal deformation errors.

3.3.3. Active Optics

Figure 10 shows the complete optical layout for the MPI Michelson interferometer and pseudo-star.⁶ The stellar source, a HeNe 633 nm laser, is located on a passively-isolated, four meter optical table. This beam is split and directed with flat mirrors to the respective testbed collecting apertures. Starting with each collecting aperture (or siderostat) the stellar light bounces off twelve surfaces (including the delay lines) in each interferometer arm before entering the fringe detector. This sensor provides the output signal for the disturbance transfer function measurement (see Figure 8).

The interferometer must equalize the two optical paths (distance from the star, through each interferometer “arm” to the interference detector) to a small fraction of the wave length of light being observed. The active optics solution to this problem is to measure the optical path difference with the fringe detector (sensor) and subsequently introduce a delay into one of the interferometer “arms” to correct for the measured difference. This is done by linearly translating an optic called the delay line (actuator).

The delay line optical assembly contains a six-inch parabolic primary mirror and a small half-inch flat secondary mirror. Collimated light entering the assembly reflects off of the primary, the secondary, and the primary again, returning collimated and parallel to the input direction but displaced vertically. Although both arms of the interferometer contain a delay line, only one needs to be actively controlled in order to equalize the optical paths from the star through each arm of the interferometer to the point where they are combined. The active delay line actually consists of three actuators, each of which has a unique stroke and bandwidth. Together, these three actuators introduce the commanded optical delay into one interferometer arm with the resolution and bandwidth of the small signal actuator and the dynamic range of the large stroke actuator. The three stages are: a stepper motor for low-frequency (DC), long-travel capability (1 m); an intermediate voice-coil actuator for medium-frequency (DC – 10 Hz), medium-amplitude control (1 cm); and a reactuated piezo-electric device (PZT) for high-bandwidth (up to kHz), precise actuation (30 μ m).

The measured fringe detector signal is translated into a distance with a custom 40 bit digital laser counter board which can provide 2.5 nm resolution (8 bits fractional position) for a single pass, 633 nm laser.

This paper uses the fringe tracker control system in two configurations: 1) open loop (turned off) and 2) closed loop. The closed loop bandwidth approximates that to be used during instrument observation mode. Based on photon rates for the projected stellar sources, the expected bandwidth is approximately 300 Hz. The loop used for this paper provided over 100 dB of rejection at 1 Hz with a 0 dB frequency of 700 Hz. The distribution of labor between the two actuators directly maps to the different frequency ranges. During observation mode, the coarse delay line cart stage will be locked down. The voice coil actuator will reject disturbances from DC to 20 Hz and the PZT from 20 Hz to 700 Hz.

Since the voice coil moves the significant mass of the entire optical assembly, its plant transfer function couples with structural dynamics. The resonant frequency of the flexure mounted optical assembly is 1.15 Hz. In contrast, the PZT plant transfer function shows no sign of coupling to the structure. This decoupling is achieved by providing both the secondary mirror PZT and the reactuation PZT with the same command, allowing the reaction forces of the two PZTs to cancel.

A 16 bit digital-to-analog output board generates a voltage proportional to the laser counter value (i.e. the remaining optical path difference). This signal is the error signal for the servo and is also sent to the HP analyzer as the output signal for the transfer function measurement.

3.4. Performance Prediction Algorithm

In the analysis environment, disturbances of four HST wheels were modeled, as SIM will carry at least four reaction wheel assemblies (RWAs) for redundancy, and the HST disturbance model was available. (The actual choice of wheel type and number is yet to be made.) The wheels were assumed to be in a pyramidal configuration, i.e., the axis of

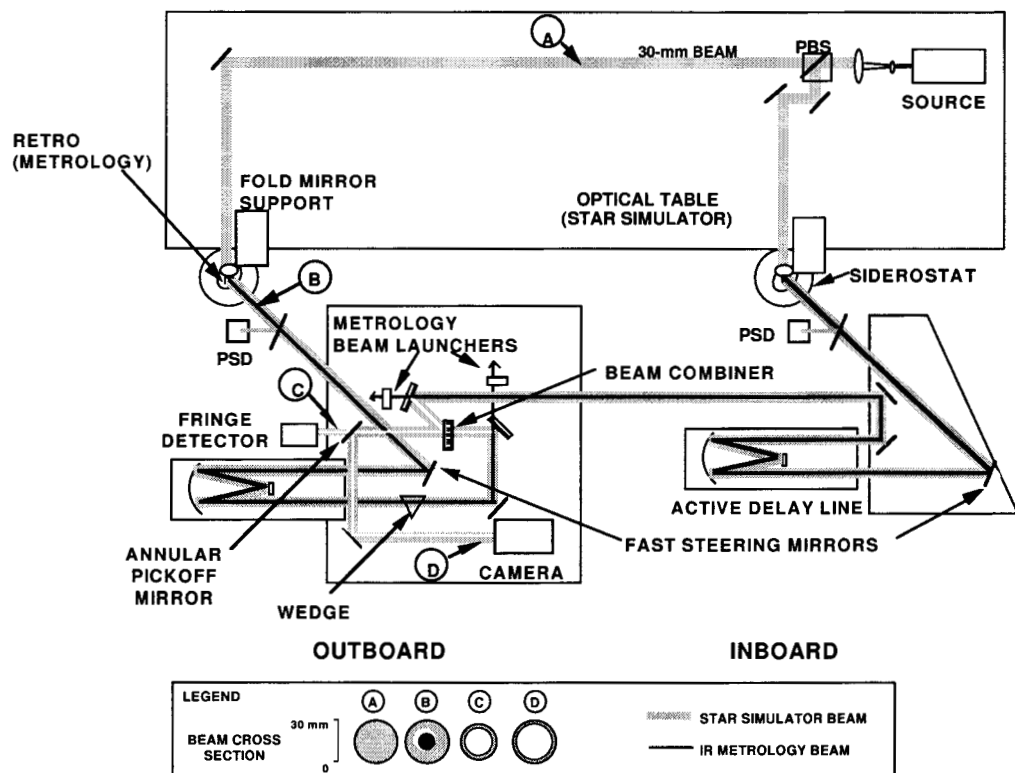
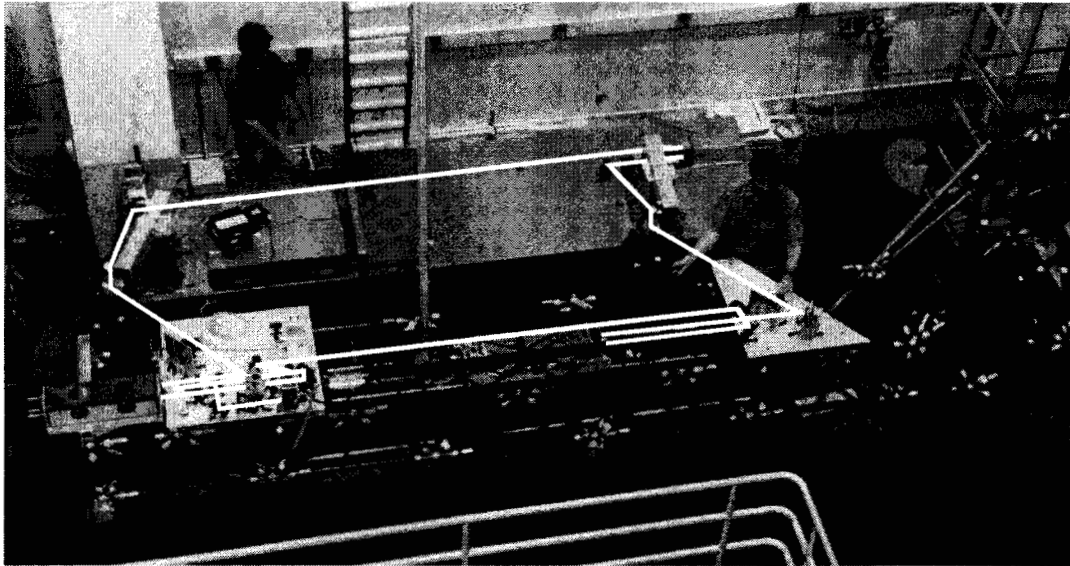


Figure 10. MPI optical layout. Block diagram identifies significant optical components. Both the block diagram and the photo depict the same region. Inset shows beam diameter at different points in the optical path.

each wheel is normal to a side of a square pyramid. The angle of the pyramid was assumed to be 63° , since this yielded equal torque capacity in all three spacecraft axes. Associated with each wheel orientation is a set of RWA local coordinates and a transformation from local to global coordinates. Applying this transformation to the disturbance transfer functions yielded transfer functions from each RWA local disturbance direction to the stellar fringe position for each RWA, as shown in Figure 6. That is, from the six global transfer functions $H_n(\omega)$, twenty local transfer functions, $\tilde{H}_{jk}(\omega)$, were created (five disturbance directions per wheel times four wheels). These twenty transfer functions were then input to the disturbance model algorithm in order to determine fringe position as a function of wheel speed.

The algorithm contains two nested loops with the outer loop indexing each wheel orientation ($k=1-4$), while the inner loop steps through all possible wheel speeds ($[f_{rwa}]_i = 1-3000$ rpm). The kernel of the algorithm is the calculation of a fringe position standard deviation, $[\sigma_{fp}]_{ik}$, for a single wheel speed (i -index) and orientation (k -index). For each wheel orientation, this calculation begins with five RWA disturbance PSD's generated from the wheel speed, f_{rwa} . These PSD's, $[\Phi_m]_{ji}(\omega)$, are multiplied by the modulus squared of their corresponding local disturbance transfer functions, $\tilde{H}_{jk}(\omega)$, and summed to yield the fringe position (optical path difference) PSD, $[\Phi_{fp}]_{ik}(\omega)$:

$$[\Phi_{fp}]_{ik}(\omega) = \sum_{j=1}^5 \left| \tilde{H}_{jk}(\omega) \right|^2 [\Phi_m]_{ji}(\omega) \quad (3)$$

An example fringe position PSD is shown in Figure 11, which contains two curves: 1) the discrete-frequency output power spectral density of fringe position as a result of a single wheel spinning at 2596 rpm; 2) the cumulative area under the power spectral density curve. The cumulative area, $[\sigma_{fp}^2]_{ik}(\omega)$, is calculated by integrating the PSD, $[\Phi_{fp}]_{ik}(\omega)$, over $[0, \omega]$:

$$[\sigma_{fp}^2]_{ik}(\omega) = \int_0^\omega \frac{1}{\pi} [\Phi_{fp}]_{ik}(\tilde{\omega}) d(\tilde{\omega}) \quad (4)$$

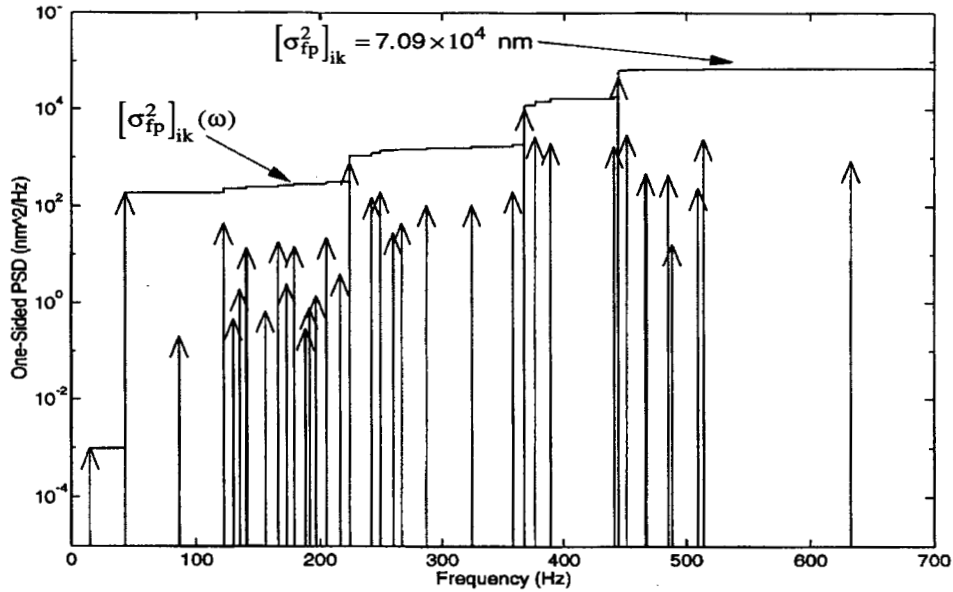


Figure 11. Fringe position power spectral density and cumulative area under the PSD curve for a wheel speed of 2596 rpm (Example for the Hard mounted configuration).

When the integration limit approaches infinity, the square root of the cumulative PSD is the fringe position standard deviation, $[\sigma_{fp}]_{ik}$, for a given wheel speed and orientation. This value ($[\sigma_{fp}]_{ik}$) represents a single point in the plot of fringe position variation as a function of wheel speed (RPM). This procedure produces four functions of σ_{fp} vs. f_{rwa_k} , one for each of the four wheel orientations, k . For a given plot, each point represents the standard deviation of a discrete-frequency power spectral density. It is not meaningful to combine these four functions into a single plot of σ_{fp} vs. a single wheel speed, since the four wheel speeds are generally not equal.

3.5. Optical Performance Metric

The methodology uses two metrics of overall interferometer performance: one for nominal operating conditions and one for worst case conditions. For each wheel, the worst-case metric, $[\sigma_{\max}]_k$, is the maximum $[\sigma_{fp}]_k(f_{rwa})$ over the range of wheel speeds. The nominal metric, $[\sigma_{rms}]_k$, is the root-mean-square of $[\sigma_{fp}]_k(f_{rwa})$ over the wheel speed. Both $[\sigma_{rms}]_k$ and $[\sigma_{\max}]_k$ for each of the four wheel orientations are root-sum-squared to produce a single performance number as shown in Figure 6.

It is important to note that the mean variance metric, $[\sigma_{rms}]_k$, is actually an L_2 norm:

$$[\sigma_{rms}]_k = \|\sigma_{fp}\|_{\ell_2}^2 = \frac{1}{f_{\max}} \int_0^{f_{\max}} [\sigma_{fp}]_k^2(f_{rwa}) df_{rwa} \quad (5)$$

where $\|\sigma_{fp}\|_{\ell_2}$ is the L_2 -norm and f_{\max} is the maximum wheel speed. This metric was first applied to the Focus Mission Interferometer in reference.⁴ It can be shown that $\|\sigma_{fp}\|_{\ell_2}$ is equivalent to the standard deviation of fringe position when the wheel speed is a uniform random variable over the interval $[0, f_{\max}]$. Assuming that the wheel speeds are stochastically independent, σ_{rms} can be interpreted as the result of a covariance analysis where the four wheel speeds are assumed to be uniform over $[0, f_{\max}]$. This justifies the interpretation of the mean variance metric as representing nominal operating conditions.

4. ISOLATOR PERFORMANCE ASSESSMENT

4.1. Tests Performed

Table 1 shows the matrix of tests performed in this evaluation study. The matrix is defined in terms of the state of the isolator (disturbance interface condition) and the state of the active optics. The isolator is in one of five states and the active optical pathlength control is either on or off. Assessing performance with the optics loop open enables evaluation of the isolator overall frequencies and shows how well the specific isolator does at attenuating disturbances on its own. Performance assessment with active optics loop closed shows how the isolator operates in conjunction with a complementary disturbance rejection scheme.

Optics loop	Perfect Iso.	Hard-Mount	Elastomeric	Passive Hex.	Active Hex.
Off		✓	✓	✓	✓
On	✓		✓	✓	✓

Table 1. Isolator/Optics test matrix. Check marks indicate tests performed in this study.

Fundamentally, the active optics attenuate at low frequency (up to 200 Hz) and the isolator attenuates the disturbances above 10 Hz. The condition with isolation but active optics off is traceable to the acquisition mode of the instrument. The condition with isolation plus active optics on is traceable to the observing mode.

4.2. Performance Results

A significant amount of data and processed data is associated with each test. For each test (checked box in Table 1), six disturbance transfer functions (one for each disturbance direction) are measured which constitute the input to the performance prediction algorithm. The algorithm output is four OPD versus wheel speed plots. Finally, each of these reaction wheel plots has two output performance metric values. In the interest of brevity, just a sample set of disturbance transfer functions and reaction wheel OPD plots are shown. However, all of the output metrics for each test are tabulated. The sample set of plots is shown for the passive hexapod isolator configuration with and without active optics, in comparison with the hardmount without active optics (worst case) and the perfect isolator with active optics (noise floor).

Figure 12 shows the measured transfer functions for one direction (X disturbance force) of the sample set. The passive hexapod isolator (open loop optics) transfer function approaches the hardmount transfer function below its resonances at 4-11 Hz. Indeed, at these fundamental resonances, the hexapod's response exceeds that of the hardmount. Then, the passive hexapod offers a reduction approaching 40 dB (a factor of 100) above 30 Hz compared

to the hardmount. At high frequency the passive hexapod isolator transfer function approaches that of the “perfect” isolator transfer. This follows since the passive isolator appears to follow a $1/f^2$ attenuation curve from 10 to 1000 Hz, and effectively disconnects the payload from the truss at 1 kHz. Note that active optics reduces response magnitude by 100 dB, or 5 orders of magnitude at low frequency, with diminishing returns above 200 Hz. Together active optics and passive isolation reduce transmissibility significantly from a few Hz to a kHz. However, the low and mid-frequency range transfer function of the passive hexapod isolator with closed loop optics approaches but does not reach the closed loop optics, “perfect” isolator transfer function. The difference is primarily due to the six fundamental isolator modes. At high frequency, this transfer function reaches the “perfect” isolator condition, again because the hexapod isolator has achieved significant attenuation by 1 kHz.

Considering only reaction wheel #1 out of the four, Figure 13 shows the corresponding outputs from the performance prediction algorithm. Passive isolation succeeds in reducing response an order of magnitude or more above 1500 rpm, while active optics adds a further 3 orders of magnitude disturbance rejection at low wheel speed.

Table 2 has the same format as Table 1 except it is filled with the previously defined output metrics. These values, which are derived from the reaction wheel plots like in Figure 13, provide a quick means of comparing the performance of the different isolators. The blank boxes indicate tests which were not performed. The best performance with active optics turned off is provided by the active hexapod isolator (137 nm rms for all wheels). Note that with the optics loop closed, the passive elastomeric isolator provides the best performance (1.37 nm rms for all wheels).

Optics	RWA #	Perfect Iso.		Hard-Mount		Elastomeric		Passive Hex		Active Hex	
	(<i>k</i> -index)	σ_{rms}	σ_{max}	σ_{rms}	σ_{max}	σ_{rms}	σ_{max}	σ_{rms}	σ_{max}	σ_{rms}	σ_{max}
Off	1			1093	6101	160	626	203	677	67	248
	2			1076	5291	170	737	206	731	71	257
	3			1036	6130	157	656	170	585	69	278
	4			899	4535	178	742	177	721	67	270
	All			2058	11110	333	1385	379	1302	137	505
On	1	.21	.67			.64	2.96	1.87	5.1	new	new
	2	.21	.71			.63	2.75	1.95	5.64	-	-
	3	.23	.71			.73	2.97	1.72	5.16	-	-
	4	.23	.73			.72	2.83	1.79	5.58	-	-
	All	.44	1.25			1.37	5.76	3.67	10.75	-	-

Table 2. Summary of isolator OPD performance results (given in nm).

4.3. Isolator Comparison Discussion

The best performance with active optics turned off is provided by the active hexapod isolator, as seen in Table 2. Figure 14 compares the measured transfer functions for one direction and the predicted open loop optics OPD performance for the TRW hexapod isolator in passive and active mode. The dominant disturbance path as seen in the transfer functions is in the low to mid-frequency range (i.e., below 100 Hz). Therefore, this mode is good for assessing an isolator’s low to mid-frequency performance. At the isolator resonance frequencies (4-20 Hz), the active feedback generally reduced response by a factor of 8-10, as compared to the passive hexapod. This translated into a factor of 3 performance improvement between the active and passive TRW isolator in terms of the OPD metric. Note that above 100 Hz, the performance of the two isolator configurations converge which it should above the bandwidth of the active isolator feedback loop. In addition, note from Table 2 that the elastomeric isolator performance is comparable to the passive TRW isolator in this mode. Therefore all conclusions drawn from the passive TRW isolator performances are applicable to the passive elastomeric isolator.

The best performance with active optics turned on is provided by the passive elastomeric isolator, as seen in Table 2. Figure 15 compares the active TRW isolator and the elastomeric passive isolator with active optics operational. Note that above 200 Hz, the hexapod isolator transfer function is above the elastomeric isolator. This difference was traceable to internal modes of the individual hexapod isolator struts which provide an undesirable mechanical disturbance path. This same problem does not exist with the mechanically simple cube of elastomer.

Because of the large rejection of the active optics below 100 Hz, the value-added of the active isolation at low frequency is not significant in the predicted OPD/RPM plot. On the contrary, the 10 dB rejection of the elastomeric isolator (compared with the active TRW isolator) at high frequency contributes a factor of 3 of improvement on the predicted OPD/RPM plot above 1000 rpm.

Performance of the active isolator on orbit would likely be better since there was some interaction in the vertical direction between the 6 active loops and the gravity offload, which prevented full vertical isolation from being achieved at 6 Hz, corresponding to a zero in the open loop plant transfer function. The reason that the active isolator did not perform as well as the passive hexapod with active optics on is due to the overlap in bandwidth of the two loops. The active optics overwhelmed the effectiveness of the active isolator loop essentially nulling its benefit. The active isolator makes response slightly higher at around 70 Hz, where the feedback crosses 0 dB and phase margin is small. The slightly worse response in that band, which is not substantially rejected by the active optics, made the passive hexapod slightly better than the active hexapod.

Quantifying the performance difference between these isolators and being able to explain cause of the difference is an example of the unique capabilities of this performance evaluation approach. Identifying the internal dynamics of the strut as a significant contributor to performance reduction in the high frequency range would be virtually impossible in a stand-alone test on a stiff test table or measuring transmissibilities on a flexible structure.

Isolator selection ultimately depends on the specific application. In the case of a space-based interferometer, these performance results suggest either the active TRW isolator or the passive elastomeric isolator would be best. Choosing between these two would ultimately depend on system level error budgeting. If for example the acquisition problem (active optics open loop) was deemed achievable and the observation mode (active optics closed loop) was in question of meeting requirements, then the passive elastomeric would be the proper selection.

5. CONCLUSION/FUTURE WORK

This paper presents a performance prediction procedure to evaluate six-axis isolation systems. The key feature of the approach is that the performance metric is the actual optical instrument sensor that must be stabilized. This setup is a benchmark to evaluate different isolator designs in the same dynamic environment. The procedure was applied to five different disturbance interface conditions. The resulting quantified performance values (Table 2) are most useful as a relative comparison as opposed to an absolute metric. In terms of an absolute comparison (e.g. to the 10 nm requirement) these results show what percent of the vibration attenuation challenge is left for the other approaches (e.g. active optics). Future improvements to the procedure include incorporating all six directions of information from the dynamometer, developing a narrowband performance metric procedure, displaying the output data in three dimensions (RPM vs. fringe variation vs. frequency) and improving the shaker design. Future isolator activities include design refinements of the TRW hexapod strut, the pure elastomer isolator and evaluating systems from other institutions.

ACKNOWLEDGMENTS

The research described was performed at the Jet Propulsion Laboratory of the California Institute of Technology, under contract with the National Aeronautics and Space Administration. The authors thank Rob Calvet and Jim Melody for their extensive contributions to the effort and the leaders of the Interferometer Technology Program, Bob Laskin, Jeffrey Yu, and Ben Parvin for their technical and financial support. The active/passive hexapod vibration isolator was developed and tested using TRW Independent Research and Development funds.

REFERENCES

1. M. M. Colavita, M. Shao, and M. D. Rayman, "OSI: Orbiting stellar interferometer for astrometry and imaging," in *Special Section on the Williamsburg Space Optics Conference*, 1991.
2. M. Shao and D. M. Wolff, "Orbiting stellar interferometer," in Reasenberg,¹⁷ pp. 228-239.
3. M. Shao, M. M. Colavita, B. E. Hines, D. H. Staelin, D. J. Hutter, K. J. Johnston, D. Mozurkewich, R. S. Simon, J. L. Hersey, J. A. Hughes, and G. H. Kaplan, "Mark III stellar interferometer," *Journal of Astronomy and Astrophysics* **193**, pp. 357-371, 1988.
4. R. A. Laskin and A. M. San Martin, "Control/structure system design of a spaceborne optical interferometer," in *Proc. AAS/AIAA Astrodynamics Specialist Conference*, (Stowe, VT), Aug. 1989.

5. J. T. Spanos, Z. Rahman, C.-C. Chu, and J. F. O'Brien, "Control structure interaction in long baseline space interferometers," in *Proc. 12th IFAC Symposium on Automatic Control in Aerospace*, (Ottoobrunn, Germany), Sept. 1992.
6. G. W. Neat, J. W. Melody, and B. J. Lurie, "Vibration attenuation approach for spaceborne optical interferometers," *IEEE Transactions on Control Systems Technology* **6**, pp. 689–700, November 1998.
7. J. T. Spanos, Z. Rahman, and G. H. Blackwood, "A soft 6-axis active vibration isolator," in *Proc. American Control Conference*, (Seattle, WA), June 1995.
8. G. W. Neat, J. F. O'Brien, N. M. Nerheim, R. J. Calvet, H. Singh, and S. Shaklan, "Micro-precision interferometer testbed: First stabilized stellar fringes," in Reasenberg,¹⁷ pp. 104–115.
9. G. W. Neat, A. Abramovici, J. W. Melody, R. J. Calvet, N. M. Nerheim, and J. F. O'Brien, "Control technology readiness for spaceborne optical interferometer missions," in *Proc. Space Microdynamics and Accurate Control Symposium*, (Toulouse, France), May 1997.
10. T. W. Nye, A. J. Bronowicki, R. A. Manning, and S. S. Simonian, "Applications of robust damping treatments to advanced spacecraft structures," in *Guidance Navigation and Control Conf.*, (Breckenridge, CO), 1997.
11. L. Meirovitch and H. Baruh, "The implementation of modal filters for the control of structures," in *Journal of Guidance, Control and Dynamics*, vol. 8, pp. 707–716, Dec. 1985.
12. A. J. Bronowicki, J. W. Innis, S. Casteel, G. R. Dvorsky, D. S. Alvarez, and E. Rohleen, "Active vibration suppression using modular elements," in *SPIE Smart Structures and Materials Conf.*, (Washington, DC), 1995.
13. J. W. Melody and G. W. Neat, "Integrated modeling methodology validation using the micro-precision interferometer testbed," in *Proc. 35th IEEE Conference on Decision and Control*, vol. 4, pp. 4222–4227, (Kobe, Japan), Dec. 1996.
14. A. Papoulis, *Probability, Random Variables, and Stochastic Processes*, McGraw-Hill, New York, 3rd ed., 1991.
15. C. H. Edwards and D. E. Penny, *Elementary Differential Equations*, Prentice-Hall, Inc., Englewood Cliffs, NJ, 1985.
16. L. F. Sword and T. G. Carne, "Precision truss structures from concept to hardware reality: Application to the micro-precision interferometer testbed," in *Spaceborne Interferometry*, R. D. Reasenberg, ed., vol. 1947 of *Proc. SPIE*, pp. 104–113, (Orlando, FL), Apr. 1993.
17. R. D. Reasenberg, ed., vol. 2447 of *Proc. SPIE*, (Orlando, FL), Apr. 1995.

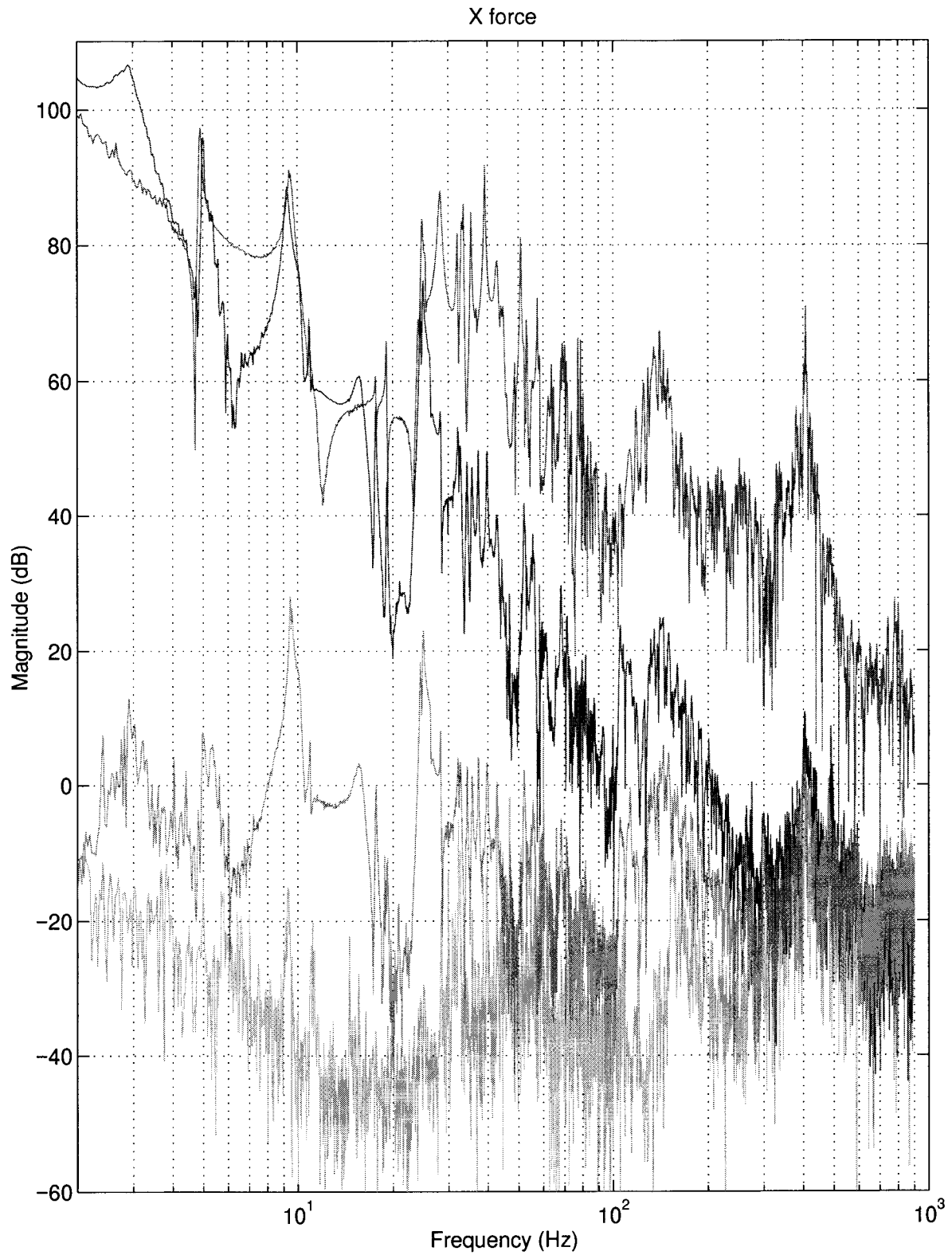


Figure 12. OPD transfer functions for X force - from the top: hardmount with active optics off, passive hexapod isolator with optics off and on, and perfect isolator with optics on.

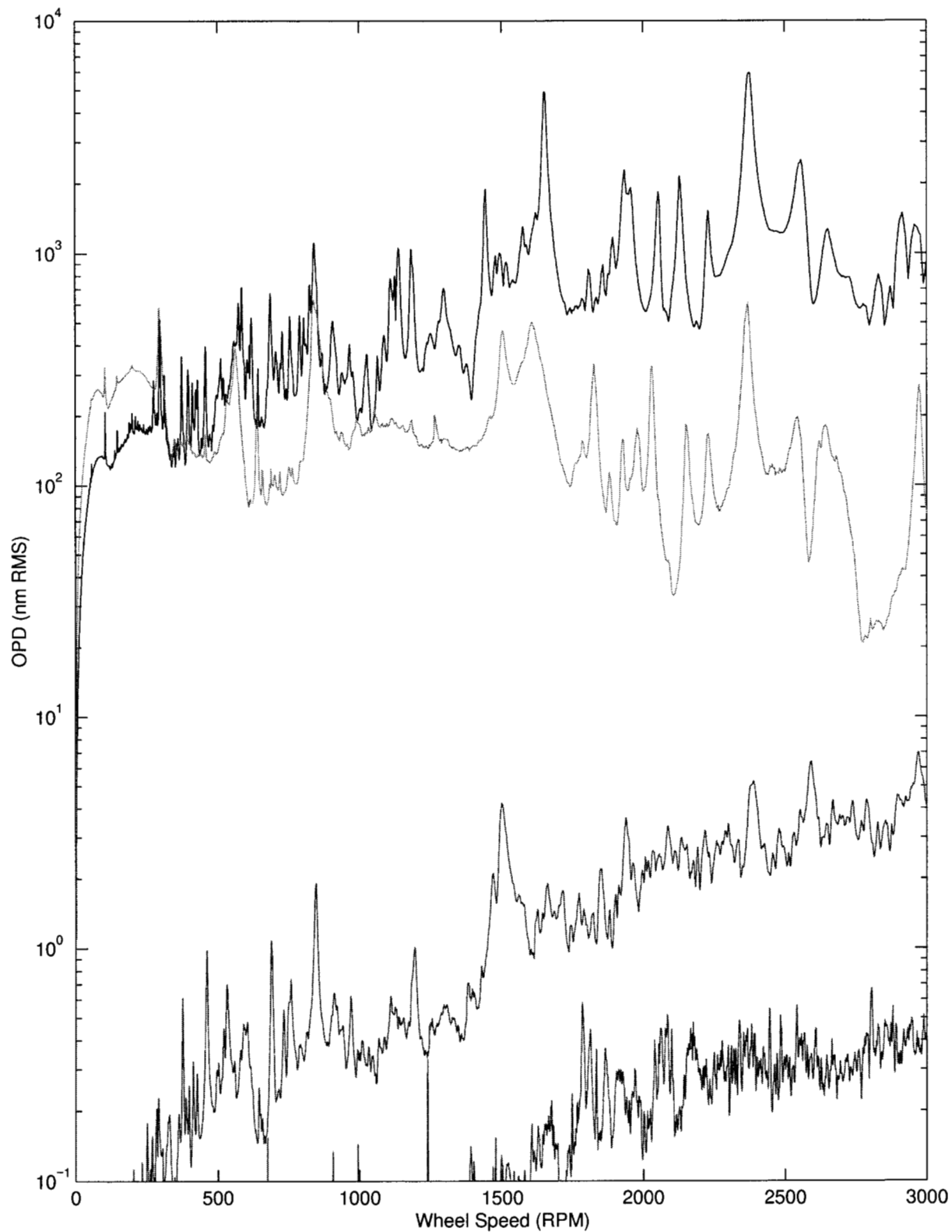


Figure 13. Predicted OPD as a function of RWA #1 speed - from the top: hardmount with active optics off, passive hexapod isolator with optics off and on or, and perfect isolator with optics on.

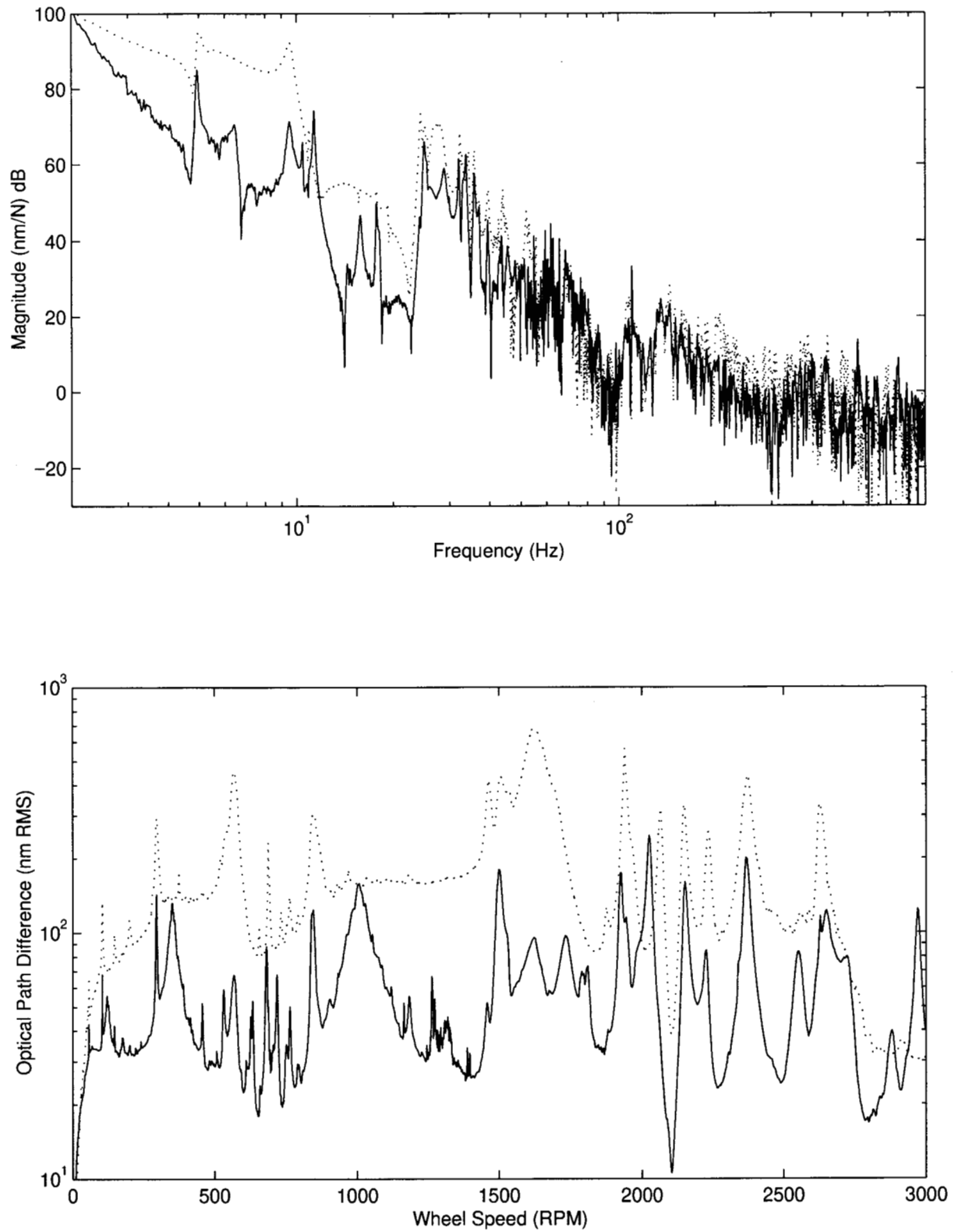


Figure 14. Disturbance transfer function (top) and Predicted OPD versus RWA #1 speed (bottom) for the active/passive TRW Hexapod Isolator (Passive Optics mode) - Dashed curves: isolator in passive mode - Plain curves: isolator in active mode.

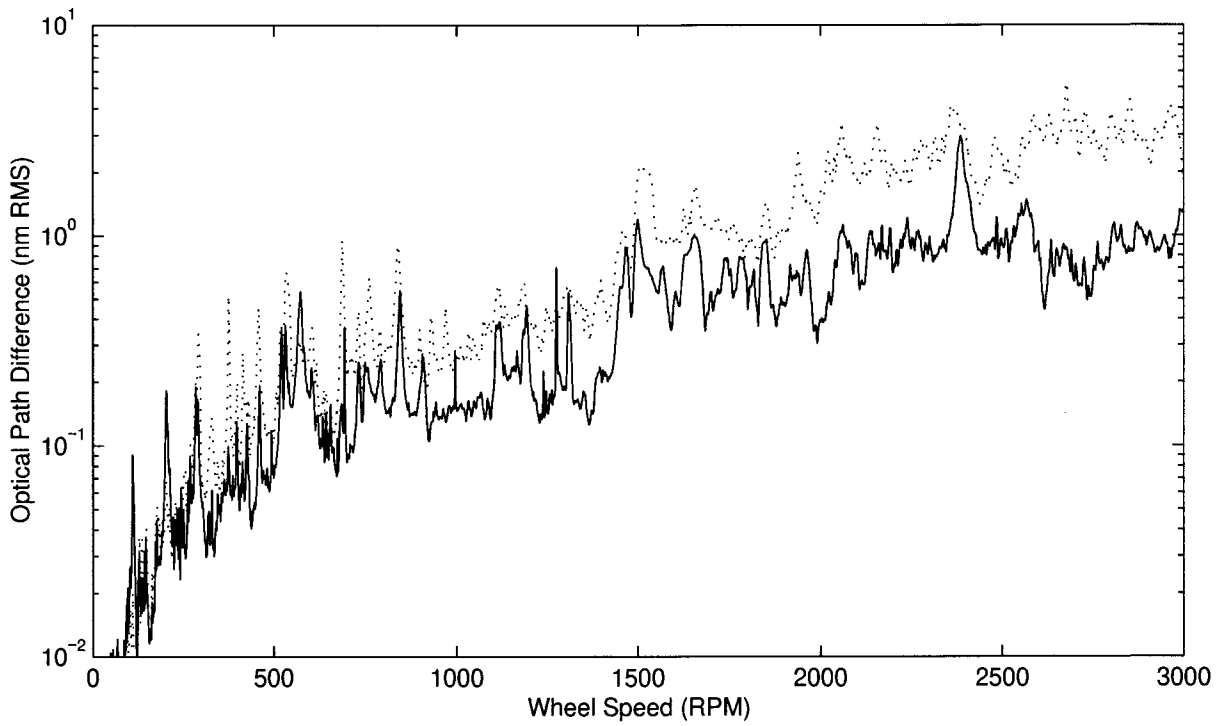
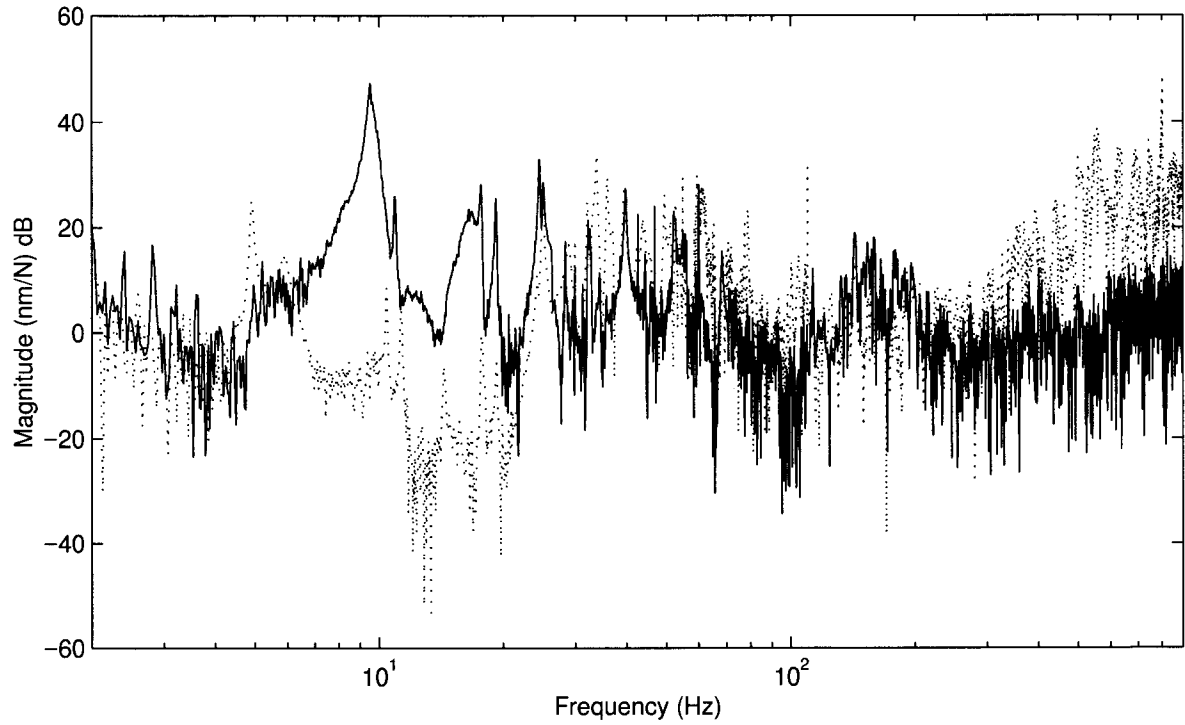


Figure 15. Disturbance transfer function (top) and Predicted OPD versus RWA #1 speed (bottom) for the active TRW Hexapod Isolator and the Passive Elastomeric Isolator (Active Optics mode) - Dashed curves: Active TRW isolator - Plain curves: Passive Elastomeric isolator.